Energies **2013**, *6*, 5507-5537; doi:10.3390/en6105507

OPEN ACCESS

energies

ISSN 1996-1073

www.mdpi.com/journal/energies

Article

An Optimization Framework for Comparative Analysis of Multiple Vehicle Powertrains

Ganesh Mohan *, Francis Assadian and Stefano Longo

Department of Automotive Engineering, Cranfield University, Bedfordshire MK430AL, UK;
E-Mails: f.assadian@cranfield.ac.uk (F.A.); s.longo@cranfield.ac.uk (S.L.)

***** Author to whom correspondence should be addressed; E-Mail: ganesh.mohan@cranfield.ac.uk; Tel.: +44-1234-754708; Fax: +44-1234-758259.

Received: 30 July 2013; in revised form: 3 October 2013 / Accepted: 7 October 2013 / Published: 22 October 2013

Abstract: With a myriad of alternative vehicle powertrain architectures emerging in the industry, such as electric vehicles and hybrid electric vehicles, it is beneficial that the most appropriate system is chosen for the desired vehicle class and duty cycle, and to minimize a given cost function. This paper investigates this issue, by proposing a novel framework that evaluates different types of powertrain architectures under a unified modular powertrain structure. This framework provides a systematic and objective approach to comparing different types of powertrain architectures simultaneously, and will highlight the benefits that can be achieved from each architecture, thus making it possible to develop the reasoning for manufacturers to implement such systems, and potentially accelerate customer take-up of alternative powertrain technology. The results from this investigation have indicated that such analysis is indeed possible, by way of identifying the "cross-over point" between powertrain architectures, where one powertrain architecture transitions into a different architecture with increments in the required travel range.

Keywords: hybrid electric vehicle; modular powertrain structure; genetic algorithm; powertrain optimization

Abbreviations:

AC	Alternating Current
AER	All Electric Range
APU	Auxiliary Power Unit
CAN	Controller Area Network

CO_2	Carbon Dioxide
CV	Conventional Vehicle
DC	Direct Current
DEFRA	Department for Environment, Food and Rural Affairs
ECMS	Equivalent Consumption Minimization Strategy
EM	Electric Machine
EV	Electric Vehicle
GA	Genetic Algorithm
HEV	Hybrid Electric Vehicle
ICE	Internal Combustion Engine
MPS	Modular Powertrain Structure
NEDC	New European Drive Cycle
OCV	Open Circuit Voltage
PHEV	Plugin Hybrid Electric Vehicle
SOC	State of Charge

1. Introduction

Stricter regulations and evolving environmental concerns have been exerting increasing pressure on the automotive industry to produce vehicles that are more fuel efficient and lower in emissions. One of the pathways to reducing road vehicle tail pipe emissions is the adoption of full-electric powertrains or hybrid powertrains (alternative powertrains). However, with a myriad of alternative powertrain configurations that currently exist within the automotive industry, choosing the most appropriate powertrain architecture for the target vehicle class and duty cycle can be challenging [1].

Hybrid electric vehicles (HEV) are becoming increasingly popular [2], driven by the notion of reduced running costs due to lower fuel consumption, when compared to a conventional vehicle (CV) with an internal combustion engine (ICE). However, the level of advantage that is gained from reduced fuel consumption is dependent on how the vehicle is used, with significantly higher fuel savings realized in city driving compared to highway driving. This is a result of the increased opportunities for energy recuperation in city conditions because of higher braking occurrences and speed variations. A study carried out by Fontaras *et al.* [3] suggested that HEVs exhibited reduction in CO_2 over CVs for urban cycles. However, this advantage is diminished as the duty cycle approaches that of a highway pattern, *i.e.*, constant high-speed cruising. At this point, it could be argued that a CV could have similar overall fuel consumption to a HEV (for a given vehicle class) because of lower opportunities for regenerative braking and near steady-state operation of the ICE [4].

In the case of a plug-in hybrid electric vehicle (PHEV), its total mass is heavier than that of a comparable CV [5]. If the PHEV usage does not exceed its all electric range (AER), then its auxiliary power unit (APU) essentially becomes “dead weight”, because its contribution to propulsion power would be minimal. Similarly, a pure electric vehicle (EV) also becomes less suitable if the consumer requires a vehicle with a relatively long travel range and minimal refuel times [6]. Although the battery

can be sized up to meet the requirements of a long travel range, the vehicle will become heavy, and may affect other attributes such as handling and tire wear [7].

Identifying the options available in terms of powertrain architectures and quantifying the benefits that can be achieved makes it possible to develop the reasoning for manufacturers, and hence potentially accelerate the implementation, and customer take-up, of alternative powertrain technology [8]. Therefore, the objective of this paper is to identify the "cross-over point" between powertrain architectures. The cross-over point is defined as the point in which one powertrain architecture transitions into a different architecture; for example with increments in the required travel range.

Using the methodology proposed in this paper, it is now possible to explore the relative characteristics and performances of multiple types of powertrain architectures simultaneously. In most literatures, such analyses were often carried out by comparing only limited types of powertrain architectures at a time [1,9–11]. Collating results from these literatures often produce findings that were discontinuous, which made it difficult for drawing conclusions when comparing multiple types of powertrains.

To investigate and identify the "cross-over point", we have developed a novel framework for the comparative analysis of powertrain architectures. Contrary to what has been done so far, this framework combines an optimization algorithm with a modular powertrain structure (MPS), which facilitates the simultaneous approach to comparing multiple types of powertrain architectures. The use of this framework will provide a clear evaluation of each type of architecture, and illustrates the potential impact of powertrain selection towards a given cost function. This framework underscores the novelty of this paper, and expands on the work published by Mohan *et al.* [12] for optimizing EV powertrains. To test this framework, the following powertrain architectures will be evaluated:

- conventional powertrain with an ICE;
- full-electric powertrain (as used in an EV);
- series plug-in hybrid powertrain (as used in a PHEV).

The goals of this investigation are two-fold:

- select the most appropriate powertrain architecture for a given vehicle class and duty cycle;
- optimize the component sizes within the powertrain architecture for a given cost function.

This paper is structured as follows: Section 2 covers the methodology of the investigation, whilst Section 3 shows the development of the powertrain components, vehicle model, and drive cycles. Section 4 then discusses further on the three powertrain architectures that are used as part of the investigation, and leads to Section 5 that discusses their implementation into the MPS. This is then followed by Section 6 with results and Section 7 with conclusions.

2. Methodology

All powertrain components were created in Matlab and Simulink, and will be described further in the next section. Each powertrain component is treated as a module and is designed to be modular and scalable in implementation, an example of which was shown by Mason *et al.* [13]. This allows the powertrain components to be interchangeable, and when coupled with an optimization algorithm, forms the framework required to achieve the goals stated in the introduction of this paper.

To utilize the framework, the details of the target vehicle class and duty cycle are required. The vehicle class is described by the following information:

- glider mass (mass of the vehicle without powertrain components);
- aerodynamic properties;
- tire rolling resistance characteristics.

The duty cycle consists of a speed trace and, optionally, information on geographical elevation.

With reference to the vehicle class and duty cycle, the proposed framework will select the most appropriate powertrain configuration using components from its database, and co-optimize those component sizes for a given cost function.

3. Model Development

To allow for modular implementation of the powertrain components, the communication between each component has to be standardized. This is achieved using power bonds, similar to the concept of Bond Graphs [14]. The MPS, which then facilitates the interchangeability between these components, is discussed further in the next section.

The following components will be included into the framework:

1. ICE;
2. EM;
3. battery;
4. APU;
5. fuel tank;
6. battery charger.

Items 1–4 were based on the models published by Shankar *et al.* [5], and therefore will not be covered in detail in this paper.

3.1. ICE

The aim of the ICE model is to be scalable and sufficiently capture the operation and efficiency envelopes of an ICE. In this paper, a baseline ICE model that is naturally aspirated and spark ignited was selected, as it is widely available on the market today [15,16]. Other configurations, such as forced induction and compression-ignited ICEs are possible; however, they were not investigated further due to the lack of experimental data at this time.

The scalable ICE model was made possible using the Willan's line method, as proposed by Guzzella *et al.* [17] and Rizzoni *et al.* [18], and implemented by Shankar *et al.* [5]. Table 1 shows the terms used for calculating the ICE's power and fuel consumption.

After obtaining the torque-speed curve and efficiency map for a given ICE displacement [5], the resultant power is calculated as:

$$P_{engine} = \frac{T_e \cdot \omega_e}{\eta_e} \quad (1)$$

The mass flow rate of fuel, $\dot{m}_{fuel}$, is then calculated, where H_l is the fuel's calorific value:

$$\dot{m}_{fuel} = \frac{P_{engine}}{H_l} \quad (2)$$

The total fuel used in a drive cycle is the integration of $\dot{m}_{fuel}$ over the length of simulation time, and this calculation will be carried out in the fuel tank model (covered later).

Table 1. Terms used for engine calculations.

Term	Definition	Units
P_{engine}	Engine power	W
T_e	Engine torque	Nm
ω_e	Engine speed	rad/s
η_e	Overall engine efficiency	-
$\dot{m}_{fuel}$	Fuel mass flow rate	kg/s

3.2. EM

The EM model was developed with data obtained from the Smart Move two EV Trial [12]. The technical specifications of the smart electric drive (ED) are shown in Appendix A1, Table A1.

Similar to the ICE model, the goal of the EM model was to be scalable to meet varying power demands. The EM is a brushless DC type [19], as utilized in the smart ED. The combined EM and inverter are represented as an efficiency map and as a function of torque and speed, as shown in Figure 1. The speed, torque, voltage and current measurements of the EM were obtained from the controller area network (CAN) interface of the smart ED, and this data was used to construct this efficiency map.

Figure 1. Efficiency map from Simulink electric machine (EM) model.

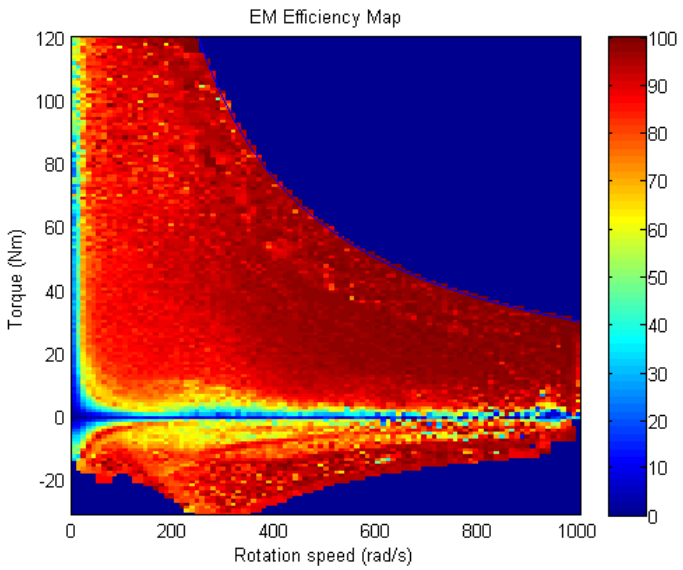

For the scope of this paper, the EM is scaled up or down by only extending or shortening the torque axis on the efficiency map. The speed axis remains the same, and the efficiency map is extrapolated as required. Additionally, a fixed regenerative braking strategy, as employed in the smart ED, is retained. In this braking strategy, the maximum amount of regenerative power is limited to 33% of the

maximum propulsion power. The available regenerative power is also phased out at lower EM speeds, as observed in the negative torque region in Figure 1, for speeds under 200 rad/s. The effects of variations in the regenerative braking strategy will be investigated as part of future research.

3.3. Battery

The battery model was created based on the work by Tremblay *et al.* [20]. The schematic representation of a single Li-ion cell within the battery model is shown in Figure 2a and consists of the open circuit voltage (OCV) connected in series with a single resistor. This relatively simple layout, also known as the "Rint" battery model [21], was adopted because the transient characteristics of the battery will be negligible given the comparatively large simulation time step of 1 s [5]. This negates the necessity to include capacitive elements (such as those found in the Thevenin battery model [21]), and hence reduces the overall simulation time.

Data for parameterization of the battery model was also obtained from the CAN interface of the smart ED. The OCV was estimated based on the battery terminal voltage, temperature, and state-of-charge (SOC). Figure 2b shows the relationship between the OCV, SOC, and temperature.

Figure 2. (**a**) Rint model for a single Li-ion cell; and (**b**) efficiency map.

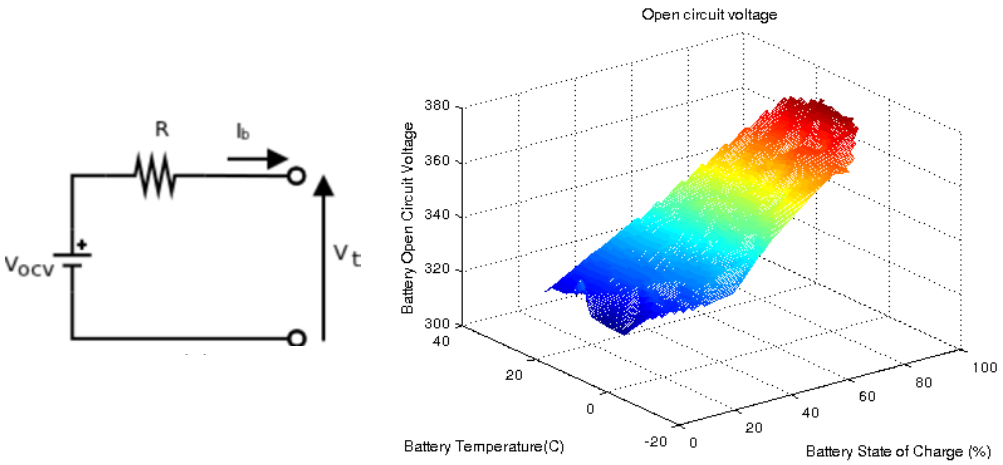

(**a**) (**b**)

To construct the battery pack model, a string of Li-ion cells were connected in series and in parallel. The cells within the battery pack are assumed to be homogeneous in operation, and this allowed for scaling the battery pack size by changing the number of parallel strings. In reality, temperature gradient and disproportionate aging may affect the performance of individual cells [22]. Each parallel string of cells has a capacity of approximately 1 kW h. Therefore, a battery pack rated at 20 kW h, for example, contains approximately 20 strings in parallel. The battery pack has an allowable operating window between 20% and 90% SOC.

3.4. APU

The APU (also called "Range Extender" in some literature [23]) is used in the series hybrid powertrain architecture, and it is formed by connecting an ICE to an EM [24]. The series hybrid architecture is discussed further in the next section.

3.5. Battery Charger and Well-to-Wheel Analysis

After completing a drive cycle, the amount of electrical energy consumed by an EV or PHEV is determined by replenishing the charge in the battery back to its initial state from the electric grid. Subsequently, the amount of well-to-wheel CO_2 emitted is then calculated by converting this consumed electrical energy into gram-CO_2 using data published by the Department for Environment, Food and Rural Affairs (DEFRA), a public UK body [25]. For a PHEV, its well-to-wheel CO_2 output combines emissions from both its electrical and fossil fuel energy sources.

According to DEFRA, the CO_2 conversion factor for electric energy produced in the UK is estimated to be 594 g CO_2/kW h for the year of 2011. However, this estimate does not include the following:

- emissions that result from commissioning and decommissioning of the electrical power plant, transmission lines, and charging station [26];
- manufacture and end-of-life disposal of the powertrain components within the vehicle.

These factors are considered beyond the scope of this investigation, but will be part of the authors' future research.

3.6. Fuel Tank

The fuel tank connects to the ICE or the APU and calculates the amount of fuel consumed. Table 2 shows the terms used for this calculation, along with calculation of well-to-wheel CO_2 emissions for usage of gasoline.

Table 2. Terms used for fuel tank calculations.

Term	Definition	Units
m_{fuel}	Fuel mass	kg
$\dot{m}_{fuel}$	Fuel mass flow rate	kg/s
TtW_CO_2	Tank-to-Wheel CO_2	kg
WtW_CO_2	Well-to-wheel CO_2	kg
WtT_CO_2	Well-to-tank CO_2	kg/J
H_l	Fuel calorific heating value	J/kg

To calculate the total amount fuel used, the mass flow rate of the fuel consumed by the ICE or the APU is integrated over the length of simulation time:

$$m_{fuel} = \int_0^{t_{end}} \dot{m}_{fuel} \tag{3}$$

The tank-to-wheel CO_2 emission is then calculated, where $mass\_ratio_{CO_2}$ is the mass of CO_2 emitted per unit mass of gasoline that undergoes complete combustion (3.17 kg CO_2/kg gasoline) [27,28]:

$$TtW\_CO_2 = mass\_ratio_{CO_2} \times m_{fuel} \tag{4}$$

Finally, the well-to-wheel CO_2 emission is calculated based on the well-to-tank conversion factor of 14.10 kg CO_2/GJ of gasoline used [25]:

$$WtW\_CO_2 = m_{fuel}(H_l \times WtT\_CO_2) + TtW\_CO_2 \tag{5}$$

3.7. Energy Supervisory Controller

For the purpose of this investigation, a thermostatic controller is used as the energy supervisory controller for the hybrid powertrain architecture because of its simplicity and well documented use in PHEVs [29,30]. The thermostat controller allows the battery to deplete from 90% to 20% SOC during charge-depleting mode, and then regulates the battery SOC between 20%–30% during charge-sustaining mode. The following are inputs and outputs of the controller:

- SOC of battery (input);
- power demand (input);
- power split (output).

However, this standardized interface allows more sophisticated controllers to be implemented in the future of this research, such as an equivalent consumption minimization strategy (ECMS) controller [31]. The authors are also considering the use of Dynamic Programming as a subroutine to optimize the trajectory of the power split between the energy converters over the duty cycle [32,33]. This subroutine can be encapsulated within the energy supervisory module.

3.8. Vehicle Model Development

A backward-facing vehicle model is used for the purpose of this investigation, and it is based on the work published by Wipke *et al.* [34]. An example of a conventional powertrain model created using the backward-facing approach is shown in Figure 3.

Figure 3. Backward-facing vehicle model with conventional powertrain.

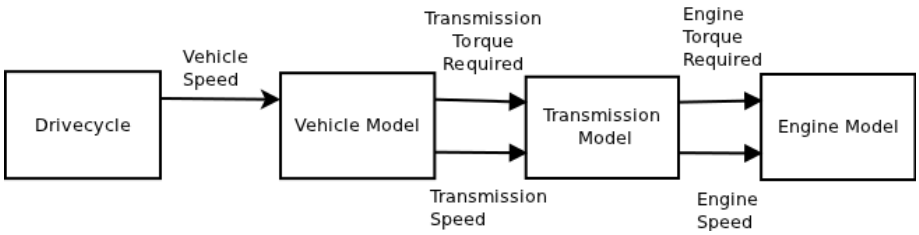

Utilization of this modeling technique permitted the use of a relatively large simulation time step of 1 s [34], resulting in quicker simulation times when compared to forward-facing models.

3.9. Drive Cycles

Three types of drive cycles were used as examples of vehicle duty cycles:

- new European drive cycle (NEDC) [35];
- real world cycle [12];
- combined Artemis cycle [12].

These drive cycles are shown in Appendix A2, Figure A1. The “Real World” cycle is derived from series of real-world EV usage studies undertaken by Cranfield University and supported by the Smart Move two EV Trial. It combines speed traces from usage in urban, A-road, B-road and motorway sections [12].

3.10. Other Assumptions and Considerations

The vehicle glider mass is assumed to remain constant at 1000 kg. The glider mass is defined as the total mass of the vehicle minus the mass of the powertrain. In reality, it may be necessary to vary the glider mass depending on the level of structural reinforcements required to support different powertrain sizes. This is considered beyond the scope of this paper.

The MPS utilizes the "switchable subsystem" in Simulink and this necessitated a uniform, power-based interface between powertrain components. To address this, the components were developed by the authors' research team, where the electrical powertrain were derived from and validated with the smart ED [4] and the ICE was validated based on the work by Guzzella *et al.* [17]. The use of this uniform power-based interface will also allow for implementation of further energy converters and energy storages in the future, such as fuel cells, flywheel, and battery models that include aging, which are currently being developed by the authors' research team.

The method of powertrain component sizing optimization used in this investigation is widely accepted within the literature [36,37]. However, it is also considered as "off-line" because the duty cycles are known a priori, and therefore the powertrain selection and sizing is fully constrained on the energy and power requirements of the duty cycle.

4. System Architectures

The high-level structure and hierarchy of the framework is shown in Figure 4. All powertrain architectures have at least one type of energy storage and energy converter respectively [24]. Using the powertrain components that were discussed in the previous section, the energy storages and energy converters are organized within the MPS, and based on this hierarchy. The optimizer interfaces with the MPS, and selects and sizes the powertrain components. The optimizer utilizes a genetic algorithm (GA), and its development will be discussed further in the next section.

Figure 4. Structure of the framework along with energy storages and energy converters.

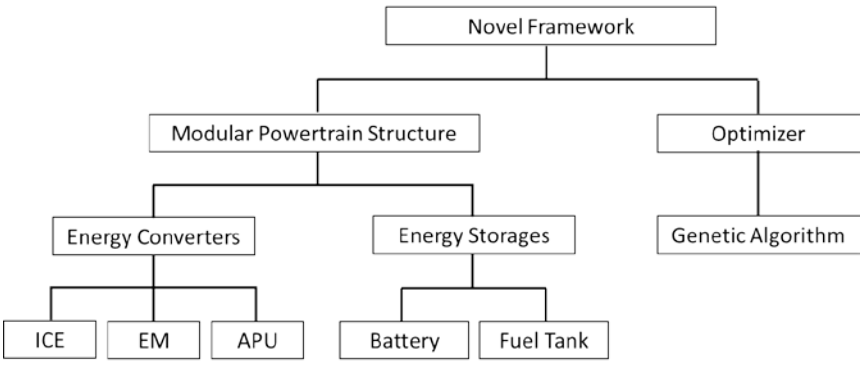

4.1. Single Source Powertrain Architecture

CVs and EVs are examples of vehicles with single source powertrain architectures. These two powertrain architectures are represented in Figures 5 and 6 respectively. In these figures, the power flow is from left to right; it begins at the energy source and flows into the "wheel". For clarity, the energy source from the electrical grid (battery charger) has been omitted in Figure 6.

Figure 5. Schematic of a conventional internal combustion engine (ICE) powertrain with transmission [24].

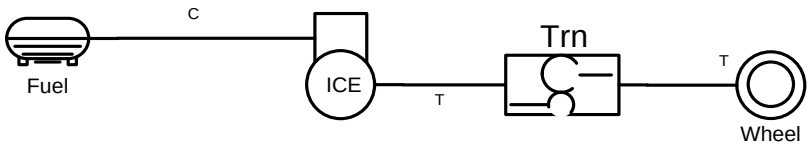

Figure 6. Schematic of a battery electric vehicle (EV) powertrain [24].

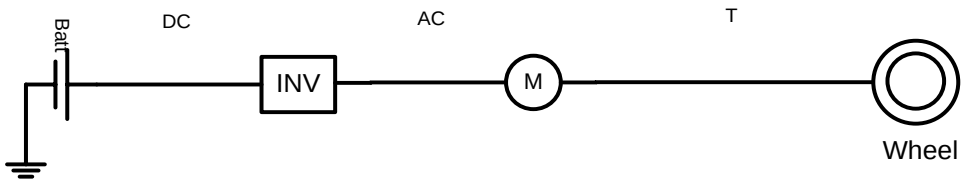

The abbreviations shown in Table 3 apply to these figures.

Table 3. Abbreviations used for diagrams.

Term	Definition
C	Chemical energy
DC	Direct Current
AC	Alternating Current
T	Torque
Trn	Transmission
INV	Inverter
M	Electrical Machine
Batt	Battery Pack

4.2. Series Hybrid Architecture

The series hybrid architecture is defined as having two (or more) power sources that are connected electrically, via an electric bus or "DC bus" [38]. Series HEVs have dedicated electric drive(s) which draws electrical power from this DC bus. Usually, one of the energy sources is rechargeable (such as a battery or ultracapacitor), whereas the other energy source is non-rechargeable (such as the fuel tank).

The hybrid powertrain used in this investigation is a series of hybrid architecture with plug-in capability, as outlined by Chan [6], and shown in Figure 7.

Figure 7. Schematic of series hybrid architecture with auxiliary power unit (APU) and battery.

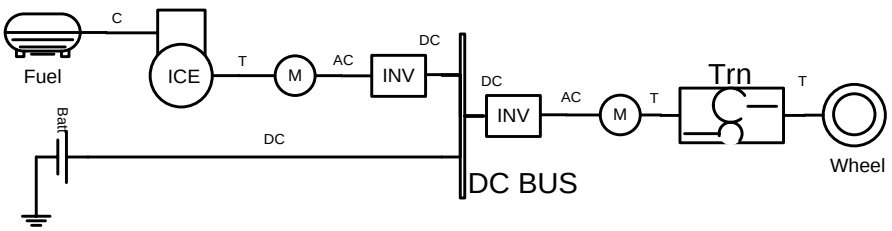

The drive system (downstream of the DC bus) is an electric machine coupled with power electronics (INV). Similar to Figure 6, the energy path from the electrical grid has also been omitted for consistency.

5. Optimizer Development

The MPS is the backbone of this investigation, and when coupled with an optimizer, forms the framework that underscores the novelty of this paper. The relationship between the MPS and the optimizer was shown in Figure 4. The MPS facilitates switchable powertrain architecture during the optimization, and for this investigation, it is capable of switching between three variants of powertrain architecture as shown in Table 4.

Table 4. Powertrain architectures simulated by model framework.

Component	Single power source		Series hybrid
Architecture Type	Conventional (Variant 1)	EV (Variant 2)	PHEV (Variant 3)
Energy converter #1	ICE	EM	EM
Energy storage #1	Fuel tank	Battery	Battery
Energy converter #2	-	-	APU
Energy storage #2	-	-	Fuel tank
Reference	Figure 5	Figure 6	Figure 7

The key feature of the MPS is the layout of the powertrain component placeholders, which can be seen in the high-level block diagram in Figure 8. This feature allows permutations of different energy converters and energy storages. This was made possible by having a clear distinction between the energy storage and energy converter, as discussed in the previous section, as well as the power transformer (consisting transmission/gearbox). The full implementation of the MPS in Simulink can be seen in Appendix A3, Figure A2.

Figure 8. High-level block diagram for layout of the powertrain component placeholders in the modular powertrain structure (MPS).

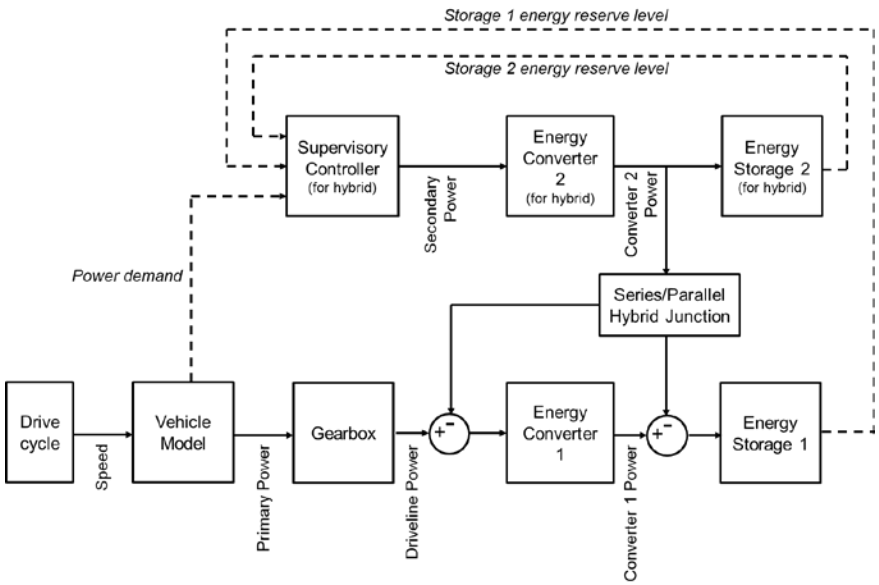

5.1. Optimizer Algorithm

Discontinuities and non-linarites will inevitably be present during the optimization routine, especially when switching between the three variants of powertrain architecture. This entails an optimizer that is non-gradient-based. Therefore, a GA type optimizer was utilized for this purpose. It has been observed that the GA is a widely used tool to optimize complex constrained non-linear problems within the domain of automotive powertrain sizing [11,39–41].

The optimizer is responsible for sizing the powertrain components and for selecting the most appropriate powertrain architecture to minimize the cost function, ϕ, as defined in the next section.

A description of the GA was covered in detail by Goldberg [42], and this technique will be extended for the use of powertrain selection and sizing. The GA initiates by seeding a homogeneous population of "individuals", spread over a solution space that is bounded by the constraints of the decision variables. The decision variables are:

- energy converter size (normalized from 1% to 100%);
- energy storage size (normalized from 1% to 100%);
- powertrain variant (one to three, as shown in Table 4).

Therefore, each individual, *X*, contains three decision variables, which can be denoted as an array in the form of Equation (6):

$$X = [\text{energy converter size, energy storage size, architecture variant}] \quad (6)$$

Each "population" will then be a collection of individuals. Each "generation" contains one population. For each generation, inferior powertrain configurations are discarded, leaving only good and feasible configurations to be selected into the next generation, thus adhering to the principles of natural selection in the GA. The normalization of the powertrain components are shown in Table 5.

Table 5. Normalization of powertrain component sizes for optimizer.

Powertrain component	Dimension	Minimum size (1%)	Maximum size (100%)
ICE	displacement	0.5 L	5 L
EM	power	10 kW	100 kW
Battery	capacity	8 parallel strings (~8 kW h)	80 parallel string (~80 kW h)
APU	power	10 kW	100 kW
Fuel tank	capacity	10 L	100 L

6. Results

The investigation methodology for testing the framework is shown in Figure 9. The purpose of "Case Study 1" is to illustrate the operation of the GA alone, and how it optimizes powertrain component sizing for a given cost function. Therefore, the powertrain switching capability within the MPS is disabled for this case study, and locked to only the EV powertrain architecture.

After reviewing the results from the this first case study, the purpose of "Case Study 2" is to then showcase the complete workings of the novel framework for comparative analysis of powertrain architectures. Therefore, the MPS is unlocked in this second case study, and all three powertrain architecture variants (shown in Table 4) are evaluated.

Figure 9. Investigation methodology for testing the framework.

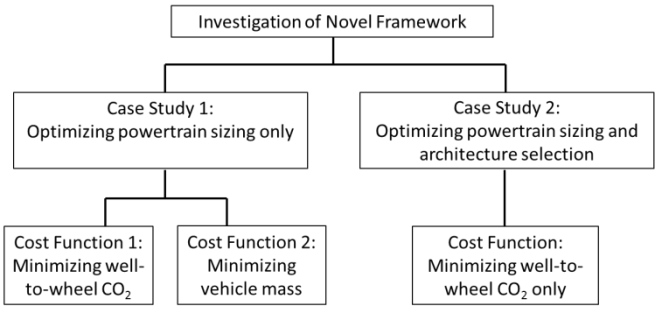

6.1. Further Drive Cycle Analysis

As discussed previously, there are three types of drive cycles that are being used to evaluate the powertrain architectures. Each drive cycle has a different range:

- NEDC (11 km);
- real world (29.8 km);
- Artemis (73 km).

To evaluate the vehicle performance over an extended range, each drive cycle was repeated back-to-back. An example is shown in Appendix A2, Figure A1, where the NEDC was repeated twice.

Based on Figure 10a, the Artemis cycle has the highest top speed whist the Real World cycle has the highest average speed. The NEDC has the largest discrepancy between top speed and average speed.

Figure 10. Comparison of speed and acceleration in each drive cycle: (**a**) maximum and average speeds; and (**b**) peak accelerations.

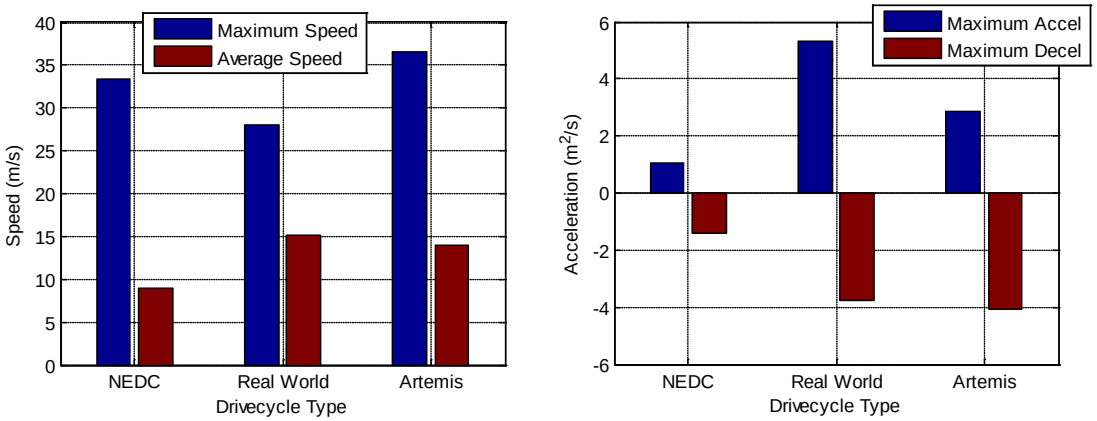

When observing the acceleration profiles in Figure 10b, the Real World cycle has the highest acceleration level, whilst the Artemis cycle has the highest deceleration level. The NEDC has the lowest peak accelerations, but has similar average acceleration and deceleration levels to the real world cycle, seen in Figure 11a.

Figure 11b shows the spread of acceleration occurrences for the three drive cycles. It is observed that the NEDC is less transient than the Real World and Artemis cycles. Based on Figure 11b, the real world cycle would require a powertrain with an energy converter (EM or ICE) that has a relatively

higher power output when compared to the other drive cycles. This is to allow the vehicle to sustain a larger spread of positive acceleration. In any case, both Real World and Artemis cycles provide more opportunity for regenerative braking when compared to the NEDC, due to the larger spread of deceleration events.

Figure 11. Analysis of accelerations in each drive cycle: (**a**) average accelerations; and (**b**) spread of acceleration occurrences.

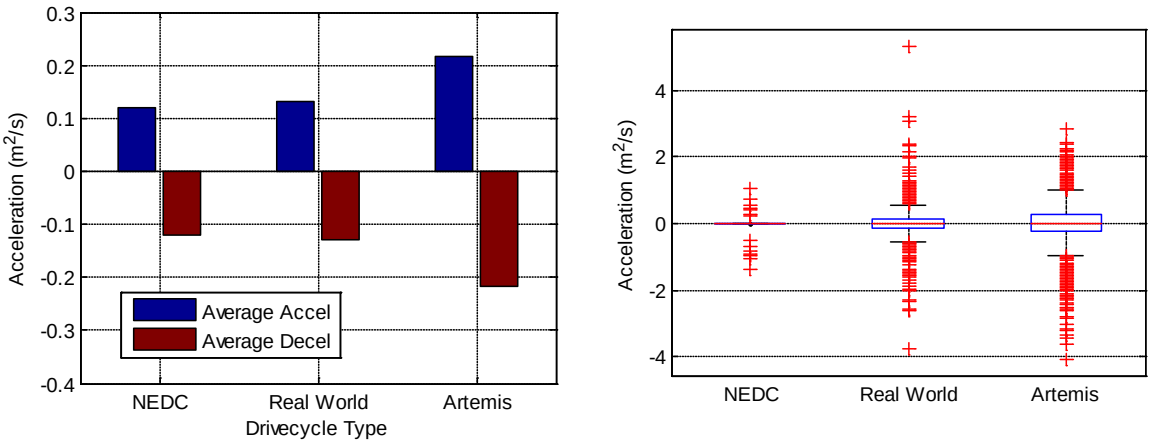

(**a**) (**b**)

6.2. Case Study 1: Optimizing Powertrain Sizing Only

In this case study, only the EV powertrain will be optimized for each of the three drive cycles. Within this case study, two investigations were carried out using the following cost functions [31]:

1. minimizing well-to-wheel CO_2;
2. minimizing vehicle mass.

Each cost function was evaluated separately. The decision variables (X) and constraints (G) are shown in Table 6.

Table 6. Decision variables (X) and constraints (G).

Term	Definition	Units
X	No. of battery strings in parallel	-
	EM size	kW
G	1000 < total vehicle mass < 2000	kg
	10 < EM size < 100	kW
	8 < battery strings in parallel < 80	-

After completing the simulations, there were differences observed in the powertrain sizing as a result of the two different cost functions, and this will be discussed next.

6.2.1. EV Powertrain Optimized for Lowest Well-to-Wheel CO_2

In this investigation, the cost function (ϕ) is well-to-wheel CO_2. The results of the optimization are shown in Figures 12 and 13. It is noteworthy that for a total vehicle mass limit of 2000 kg, the shortest

travel range is achieved during the Artemis drive cycle. Similarly, the highest well-to-wheel CO_2 emission also points to the Artemis drive cycle.

Figure 12. Optimization results for lowest well-to-wheel CO_2: (**a**) battery pack size; and (**b**) EM size.

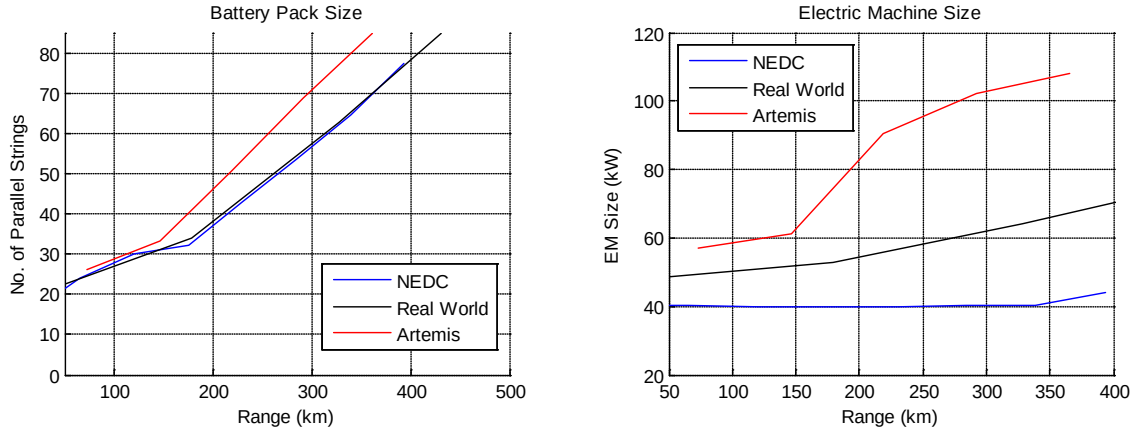

(**a**) (**b**)

Figure 13. (**a**) CO_2 emission per km; and (**b**) vehicle mass when optimized for lowest well-to-wheel CO_2.

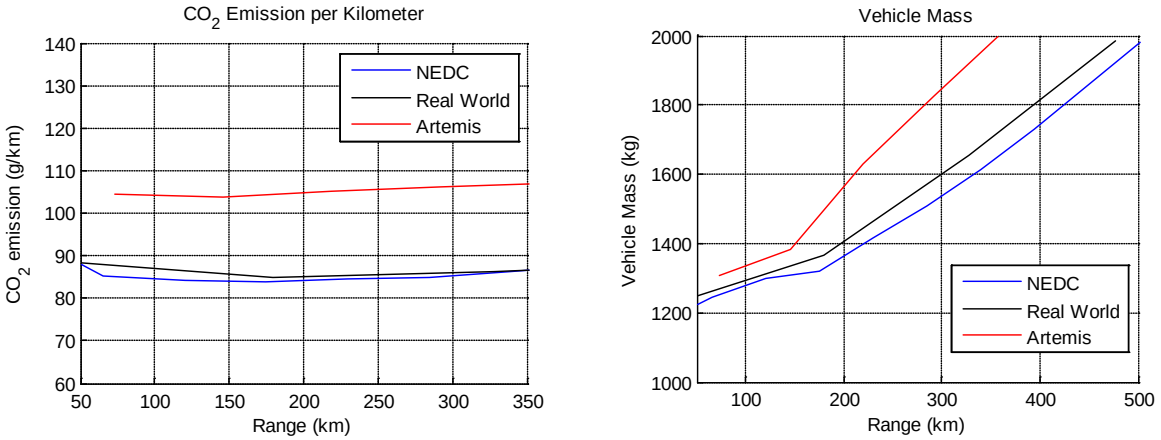

(**a**) (**b**)

The battery sizes between the Real World cycle and the NEDC were comparable because of similarities in the net amount of energy required to complete these drive cycles for a given range (approximately 6 MJ for the first 10 km). This correlates with the observation made in Figure 11a, where the NEDC has similar average acceleration and deceleration levels to the Real World cycle. Conversely, the size of the EM is different due to higher absolute acceleration level in the Real World drive cycle when compared to the NEDC, as seen in Figure 10a.

6.2.2. EV Powertrain Optimized for Lowest Vehicle Mass

In this investigation, the cost function (ϕ) is vehicle mass. The two most significant results are shown in Figure 14; battery pack size and total vehicle mass. It is noteworthy that the batteries start at a lower pack size in Figure 14a, when compared to that shown in Figure 12a. This will be discussed in

the next section. Other trends are observed to be similar between the two cost functions, with the vehicle optimized for the Artemis drive cycle once again having the lowest travel range for a given vehicle mass.

Figure 14. Optimization results for lowest vehicle mass: (**a**) battery pack size; and (**b**) total vehicle mass.

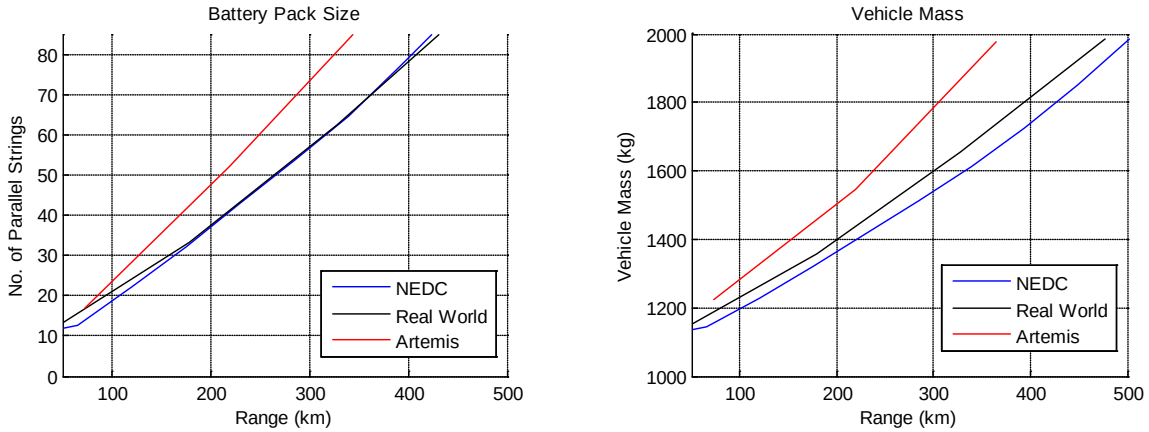

(**a**) (**b**)

6.2.3. Comparing the Results of the Two Cost Functions

The first comparison aims to identify the differences observed in the optimized EM size for the two cost functions, using the Artemis cycle as an example. Figure 15a shows the EM sizes with respect to increments in travel range, with blue and red lines reflecting optimized sizes for lowest well-to-wheel CO_2 and lowest vehicle mass respectively. When taking a travel range of 200 km as an example (green line in Figure 15a), the resultant efficiency map and scatter of EM power usage over the drive cycle is created (Figure 16). Figure 15b shows the difference in brake regeneration ability between the two different EM sizes. The EM optimized for well-to-wheel CO_2 has a higher power rating, and therefore recovers more braking energy when compared to the EM optimized for vehicle mass. This is further illustrated in Figure 16.

Figure 15. Comparison of EM characteristic over the Artemis drive cycle: (**a**) EM size; and (**b**) Percentage of recovered braking energy.

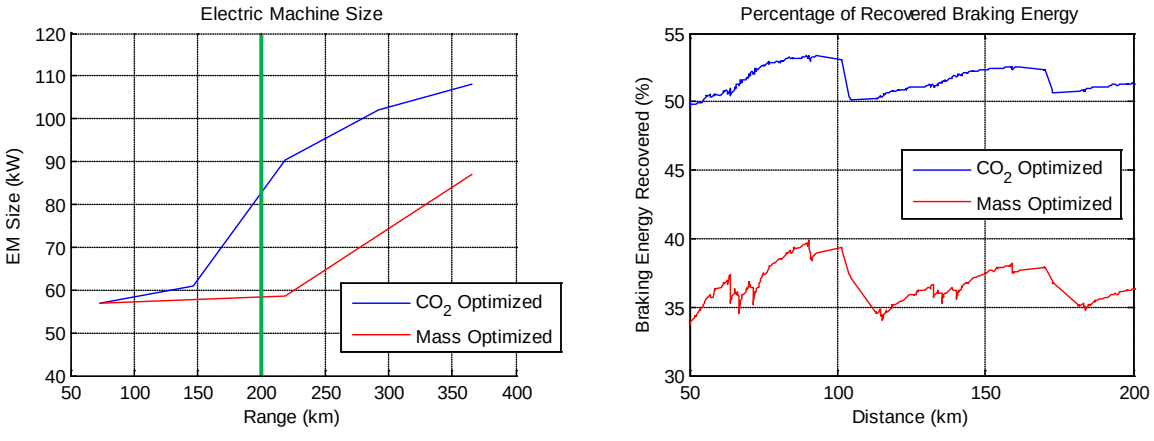

(**a**) (**b**)

The white scatters in the negative torque region are braking points encountered during the drive cycle. To minimize well-to-wheel CO_2, the EM has to recover as much braking energy as possible. Given the regenerative braking strategy imposed, this necessitated a larger EM to accommodate as much of the regenerative energy as possible.

Conversely, when optimized for smaller mass, the EM was sized just large enough to be able to handle the positive torque demands of the drive cycle, at the expense of regenerative braking abilities. This can be observed in Figure 16b, where the white scatter plots in the positive torque region are closer to the power limits of the EM.

Figure 16. Comparison of EM efficiency and usage over the Artemis drive cycle: (**a**) optimized for lowest well-to-wheel CO_2; and (**b**) optimized for lowest mass.

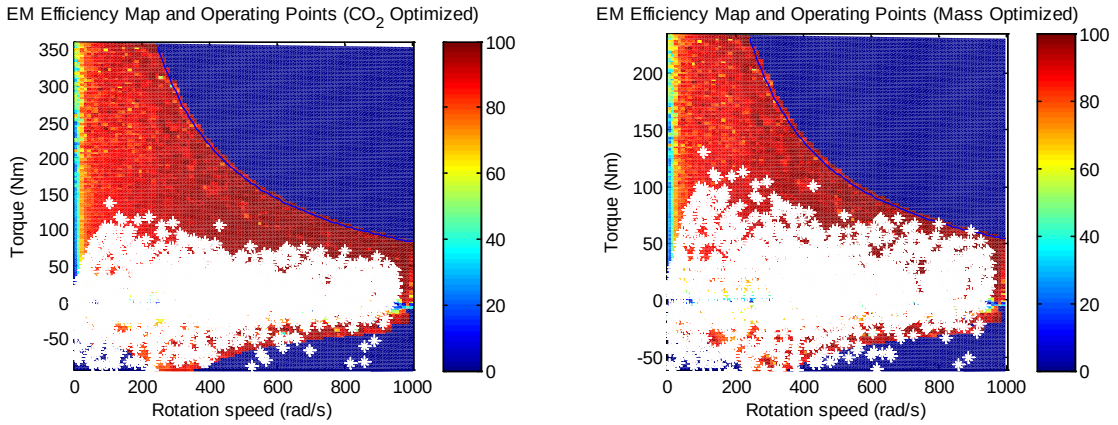

(**a**) (**b**)

The second comparison aims to identify the differences observed in the optimized battery size for the two cost functions, using the NEDC as an example. For a travel range of 66 km (green line in Figure 17a), it is observed that the vehicle that was optimized for well-to-wheel CO_2 features a larger battery pack compared to the vehicle that was optimized for mass. This is further validated in Figure 17b for the same travel range, where the vehicle that was optimized for mass has a higher CO_2 output per kilometer, despite having the smaller battery (and therefore lighter) of the two vehicles.

Figure 17. Comparison of battery pack size and CO_2 emission over the new European drive cycle (NEDC) drive cycle: (**a**) battery pack size; and (**b**) well-to-wheel CO_2 per kilometer.

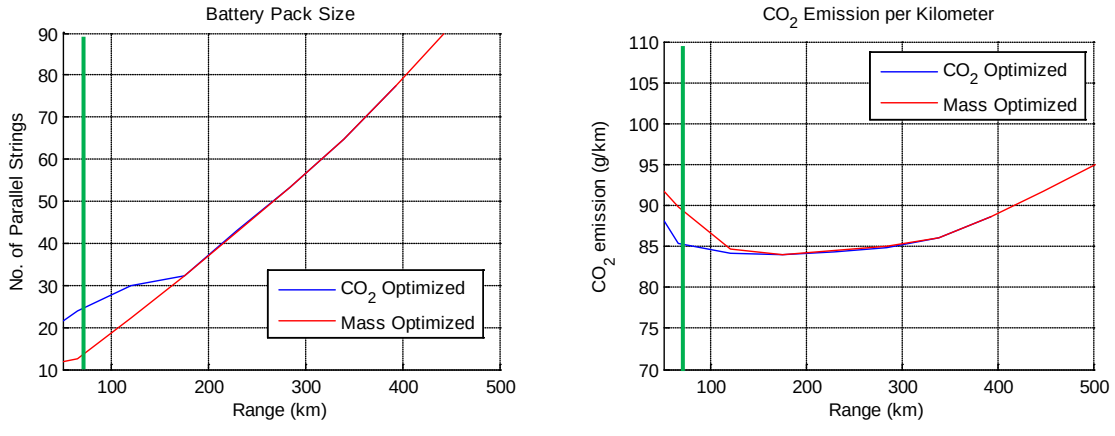

(**a**) (**b**)

The reasoning to support this finding can be inferred from the histograms in Figure 18. In Figure 18a, a smaller battery pack encounters a higher C-rate to provide the same amount of propulsion power. Therefore, although the battery pack is lighter, it is less efficient because of higher power losses associated with $P = I^2R$, where P is electrical power; I is current; and R is the internal resistance of the battery. This difference in efficiency is reflected in Figure 18b.

Figure 18. (**a**) Battery C-rate; and (**b**) efficiency histogram for EV sized for 66 km of NEDC.

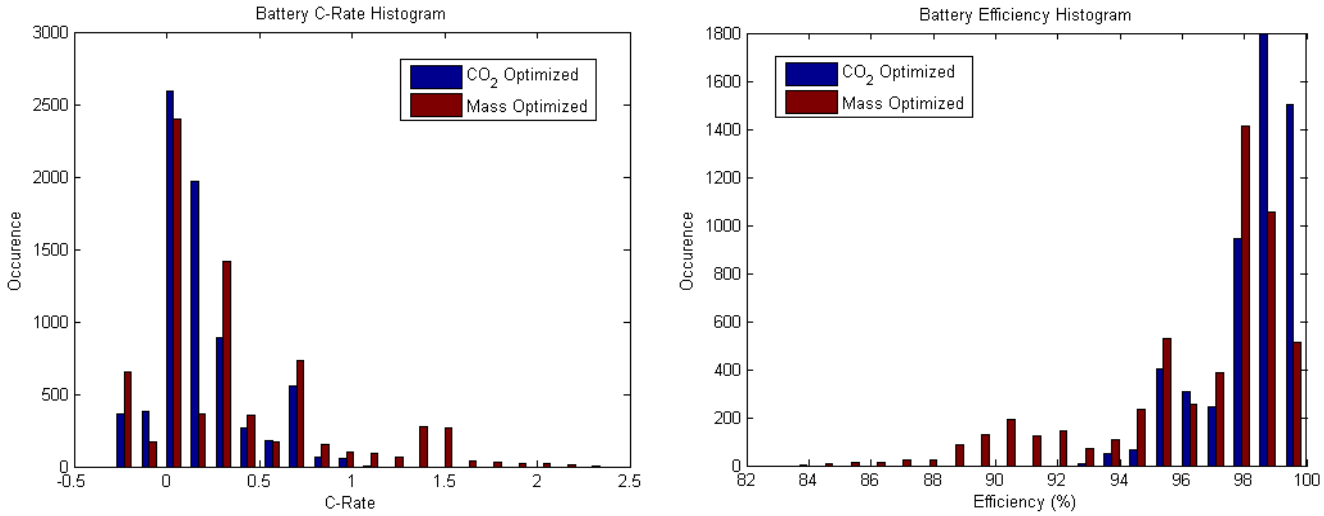

(**a**) (**b**)

However, for travel range greater than 150 km, the influence of the battery pack's mass becomes more dominant. Therefore, the resultant battery pack sizes from both cost functions converge and yield almost identical CO_2 emissions, as observed in Figure 17b. Here, it is also noteworthy that the lowest point for CO_2 output per kilometer occurs at around 175 km. This finding is not crucial for this investigation, and is therefore discussed in Appendix A4.

The results so far has given some insight on EV powertrain sizing according to drive cycle and range. In the next section, this method of optimization will be extended to other powertrain architectures, as well as giving the optimizer the ability to select the most appropriate powertrain for a given drive cycle and range.

6.3. Case Study 2: Optimizing Powertrain Sizing and Architecture Selection

In Case Study 2, all powertrain architecture variants, as listed in Table 4, will be investigated. The cost function (ϕ) is minimizing well-to-wheel CO_2 only. The framework's role is to simultaneously optimize the powertrain sizing and architecture selection, while meeting the power and energy demands of the respective drive cycle. In this case study, a total vehicle mass limit of 1600 kg is imposed, as the target vehicle class is an E-segment vehicle [43].

The simulation is run in multiples of each drive cycle, up to a maximum range of about 450 km. In each run, the powertrain is required to complete the entire range of the drive cycle.

6.3.1. Optimization for Lowest Well-to-Wheel CO_2

Based on Figure 19, the EV powertrain was selected by the optimizer for travel range increments of up to 230 km on the NEDC. In the Real World and Artemis drive cycle however, this reduces to about 210 km and 140 km, respectively.

Figure 19. Well-to-wheel CO_2/km emission: (**a**) NEDC; (**b**) real world; and (**c**) Artemis.

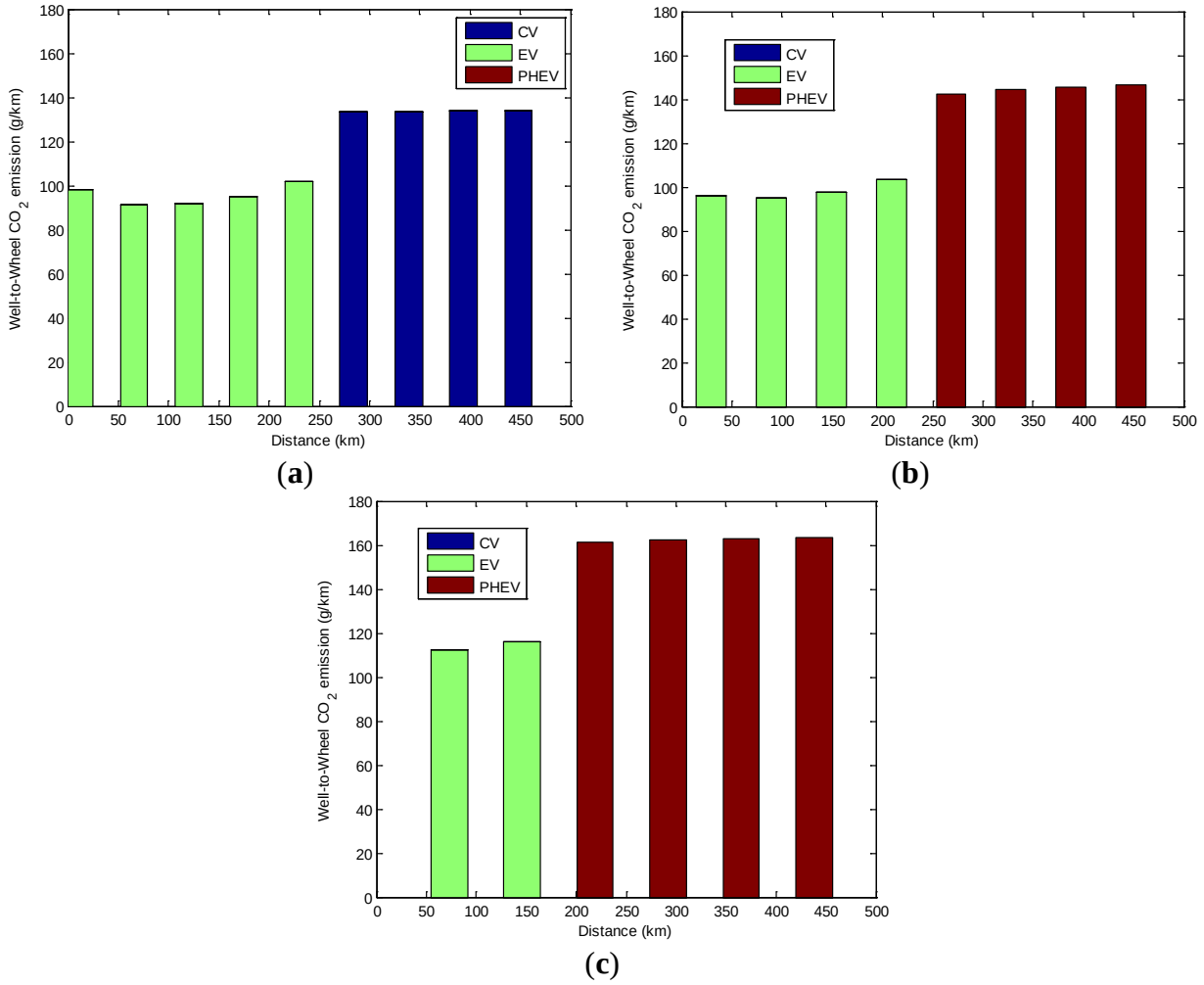

The EV powertrain offers the lowest well-to-wheel CO_2/km when compared to the CV and PHEV powertrains, for a given drive cycle and range. As a result, the optimizer has selected the EV powertrain for the initial increments of each drive cycle. The crossover from EV powertrain to a different type of powertrain occurred when the vehicle mass limit of 1600 kg was reached or exceeded. The EV powertrain could no longer support a battery large enough to cover the necessary range within the mass limit. This is observed in Figure 20, which shows the total vehicle mass of the respective powertrain and for the range that it was sized for.

To cater for a travel range of over 140 km on the Artemis cycle, for example, a vehicle with an EV powertrain would exceed the mass limit of 1600 kg. Additionally, the increase in vehicle mass as a function of travel range is steeper for the EV when compared to the CV and PHEV. This is because the energy density for batteries is smaller than that of fossil fuels by two orders of magnitude [44]. Similarly, the mass of the battery as a percentage of the total vehicle mass is greater than that of the

fuel tank. This is observed in Appendix A5, Figure A4, which shows the breakdown of the vehicle masses from Figure 20. The definitions of the respective energy converters and energy storages for each type of powertrain architecture in Figure A4 were covered in Table 4.

Figure 20. Total vehicle mass for the respective architectures selected by the optimizer. (**a**) NEDC; (**b**) real world; and (**c**) Artemis.

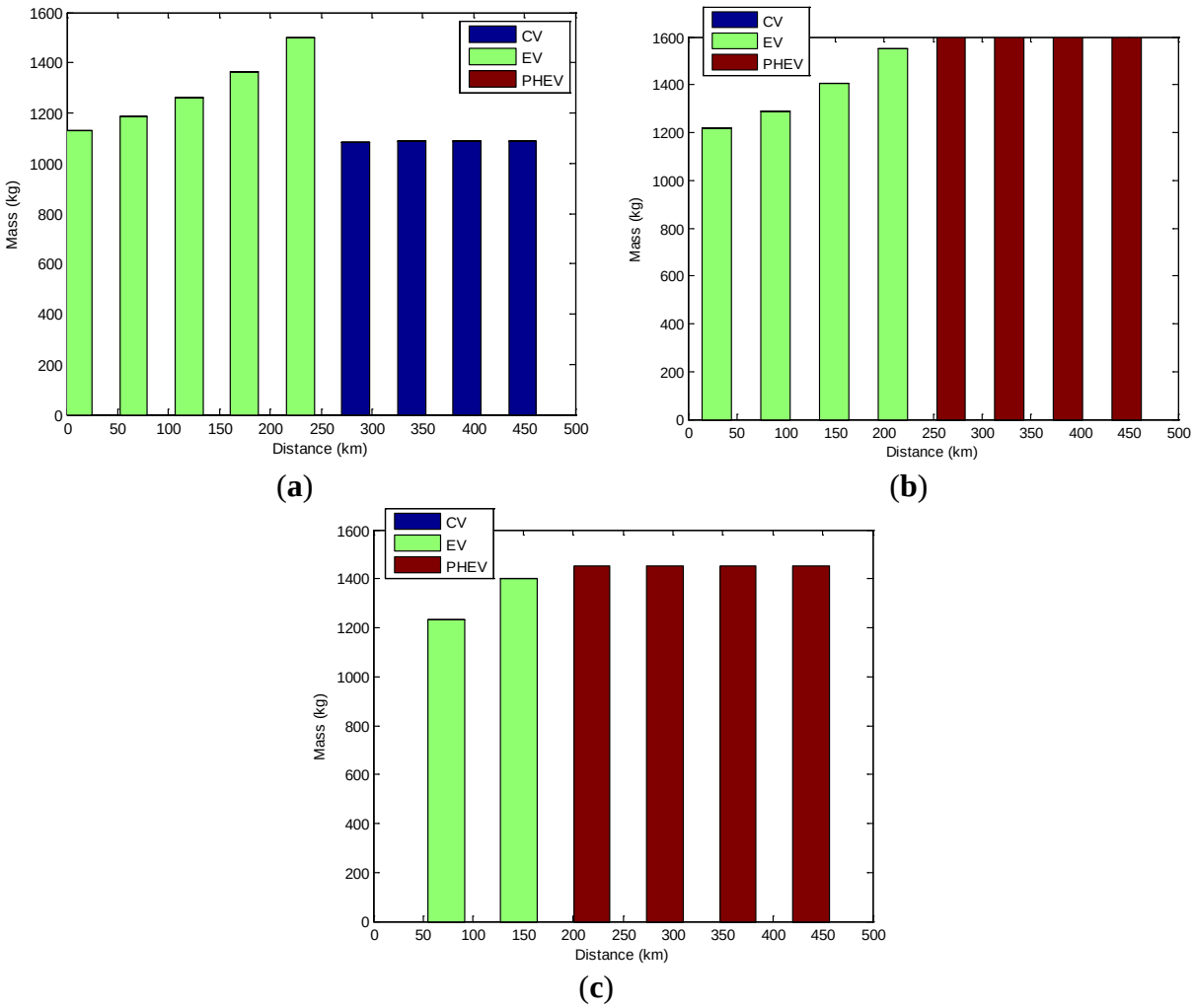

In Case Study 1, where only the EV powertrain was optimized, the results indicated that the vehicle had a longer travel range on the NEDC than the Artemis cycle for a given powertrain size, as observed from Figure 13b. This is because the overall power and energy requirements of the NEDC are lower than those of the Artemis cycle. Referring back to Figure 20, it can be inferred that this is the reason for the transition to happen at a longer range in the NEDC than in the Artemis and Real World cycles.

6.3.2. Power and Energy Analysis

As mentioned in the model development section, the current regenerative braking strategy limits the maximum amount of regenerative power of the EM to 33% of the maximum propulsion power. The regenerative power is also phased out at low EM speeds (under 200 rad/s), as seen in Figure 1. Additionally, the EM size is a decision variable for the optimizer, and it is scalable between 10 kW and 100 kW.

To minimize well-to-wheel CO_2, the EM has to recover as much braking energy as possible. Any deceleration event on the drive cycle that exceeds the maximum regenerative power of the EM will be blended with the friction brakes, which dissipate the energy to the environment as heat.

At minimum, the EM has to be sized just large enough to be able to handle the positive power demands of the drive cycle. This would result in an EM with the lowest possible mass, and subsequently allow the use of a smaller battery, due to the lower C-rates encountered. However, as discussed during Case Study 1, the disadvantage of this approach is that a smaller EM would not be able to capture all deceleration events, thus sacrificing energy that could have been recovered via regenerative braking. It is therefore the role of the optimizer to choose between the following:

- sizing the EM for lowest overall powertrain mass;
- sizing the EM for maximizing energy recovery via regenerative braking.

In Figure 21, a combination of this decision can be seen. For the Real World cycle, the EM has been sized to maximize on regenerative braking, which resulted in an EM with higher power rating than the maximum positive power encountered in the drive cycle. Conversely for the Artemis cycle, the EM was sized just enough to meet the positive power demands, sacrificing on the recuperation of braking energy. A direct consequence of this can be observed in Figure 22b,c, where the percentage of recovered braking energy in the Real World cycle is higher than that of the Artemis cycle.

Figure 21. Drive cycle and energy converter power: (**a**) NEDC; (**b**) real world; and (**c**) Artemis.

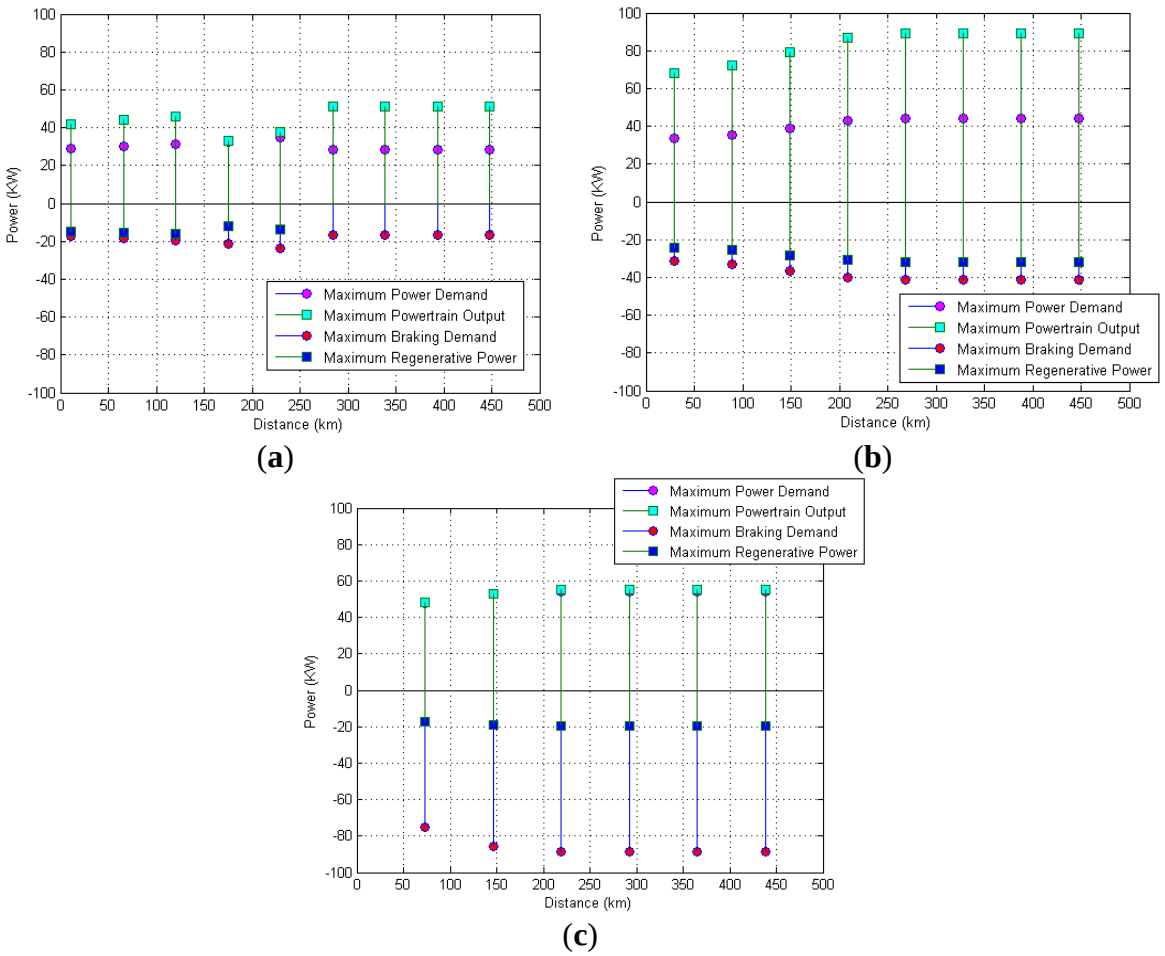

Figure 22. Percentage of recovered braking energy: (**a**) NEDC; (**b**) real world; and (**c**) Artemis.

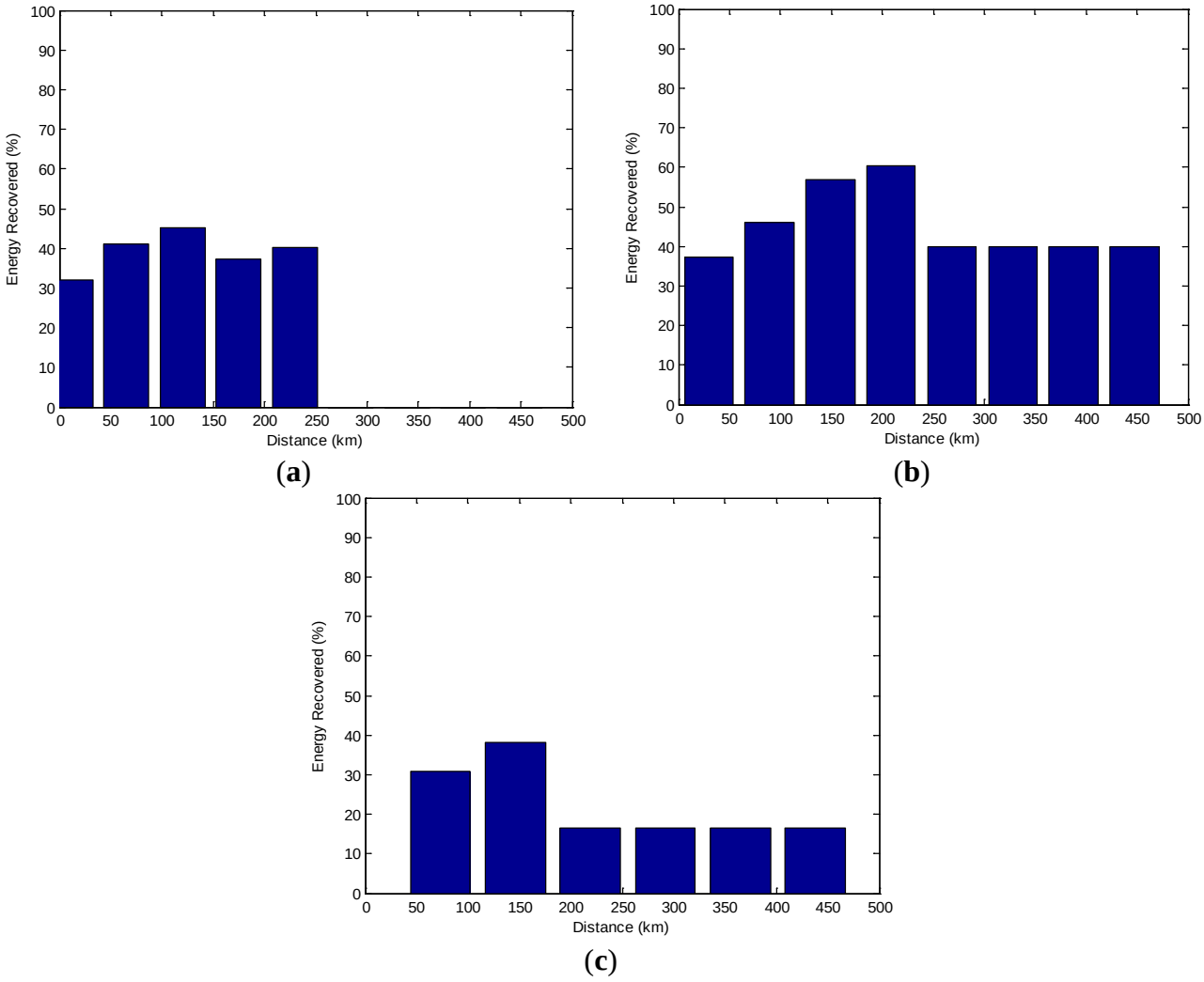

For the NEDC, the result was mixed; the EM was sized for maximum regenerative braking for travel range of up to 120 km, and then it was sized for maximum positive power thereafter, as seen in Figure 21a. After the EV powertrain transitioned to conventional powertrain, however, there was no more regenerative braking, and the ICE was sized to minimize its fuel consumption instead.

One reason to suggest the tendency of the optimizer to scale the EM for minimizing mass or maximizing regenerative braking can be inferred from Figure 23. The total energy (positive and negative) required by the Artemis cycle is higher than the NEDC cycle for a given range. This correlates back to Figure 11b, where there is a larger spread of acceleration events (evident from the longer distance between 25th and 75th percentile lines on the box plot). Therefore, sizing the EM (and subsequently the battery) to maximize braking energy recuperation in the Artemis cycle would have resulted in a powertrain that is very heavy, and this would have caused the vehicle to emit more well-to-wheel CO_2 per km, despite the increase in regenerative braking capability.

One reason to suggest the tendency of the optimizer to scale the EM for minimizing mass or maximizing regenerative braking can be inferred from Figure 23.

Figure 23. Total energy from drive cycle and recovered braking energy: (**a**) NEDC; (**b**) real world; and (**c**) Artemis.

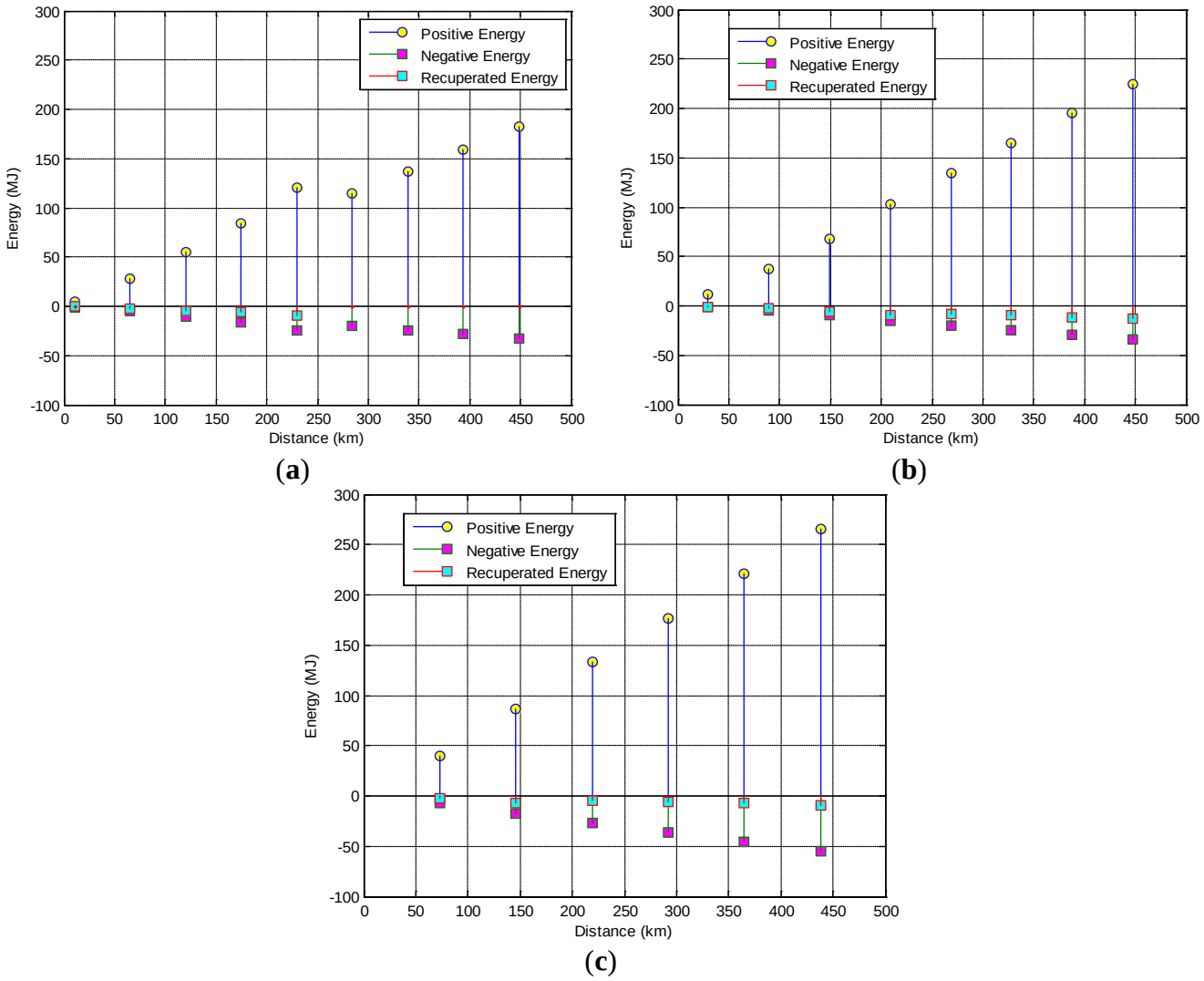

The total energy (positive and negative) required by the Artemis cycle is higher than the NEDC cycle for a given range. This correlates back to Figure 11b, where there is a larger spread of acceleration events (evident from the longer distance between 25th and 75th percentile lines on the box plot). Therefore, sizing the EM (and subsequently the battery) to maximize braking energy recuperation in the Artemis cycle would have resulted in a powertrain that is very heavy, and this would have caused the vehicle to emit more well-to-wheel CO_2 per km, despite the increase in regenerative braking capability. The authors acknowledge that the results presented here are based on the assumptions made during the development of the powertrain components. These results may vary if further uncertainties are introduced into the model, such as component degradation and performance variation caused by changes in operating temperature. Additionally, the regenerative braking strategy is expected to play an important role in deciding the point of transition between the powertrain architectures. Sensitivity studies based around these uncertainties and assumptions can be included into the framework, and are currently being investigated.

Vehicle manufacturers also use other measures such as minimum standing start acceleration times to size the powertrain components. These attributes can also be included into the framework by

supplementing the drive cycle to include such power demands. It ought to be mentioned that the well-to-wheel CO_2 data used for the generation of electrical energy was based on data from the UK grid, and therefore the results will vary based on the grid mix in different countries.

7. Conclusions

Using the novel framework proposed in this paper, investigations have identified the "cross-over point" between powertrain architectures, based on the duty cycle and required travel range. The proposed methodology, supported by this finding, opens a way for vehicle manufacturers to quantify the benefits that can be achieved from each type of powertrain architecture, and potentially accelerate the implementation and customer take-up of alternative powertrain technology. Although this investigation was limited to three types of powertrain architecture, the flexibility of the Modular Powertrain Structure will enable additional types of energy converters and energy storages to be included, thus creating further permutations of powertrain architectures. In Case Study 1, the influence of different cost functions towards powertrain sizing was more evident when the vehicle was optimized for lower travel ranges. In Case Study 2, only one cost function was used to illustrate the workings of the framework; however more comprehensive cost functions are currently being investigated as part of this research, including the use of weighted cost functions for multi-objective optimization. In Case Study 2, it was also interesting to note that the Conventional Vehicle was selected instead of the PHEV for travel ranges above 250 km on the NEDC cycle. The NEDC is a less demanding cycle when compared to the real world and Artemis cycles, and does not offer as good an opportunity for regenerative braking. As a result, using a PHEV would have resulted in a heavier vehicle without the benefits of reduced emissions.

Appendix

Appendix A1

Table A1. Data from the smart electric drive (ED) [45].

Make	Smart (Mercedes Benz)
Model	Fortwo ED (Electric Drive)
Electric machine	Zytek Automotive 55 kW (limited to 30 kW propulsion, 10 kW regenerative braking)
Battery pack	16.5 kWh Li-ion (Panasonic NCR18650 cells)
Top speed	27.7 m/s (62 miles/h)
Weight	965 kg unladen weight
Range	135 km (NEDC drive cycle)
Well-to-wheel CO_2	107 g/km (NEDC drive cycle) (DEFRA report)

Appendix A2

Figure A1. The three types of drive cycle used in the investigation.

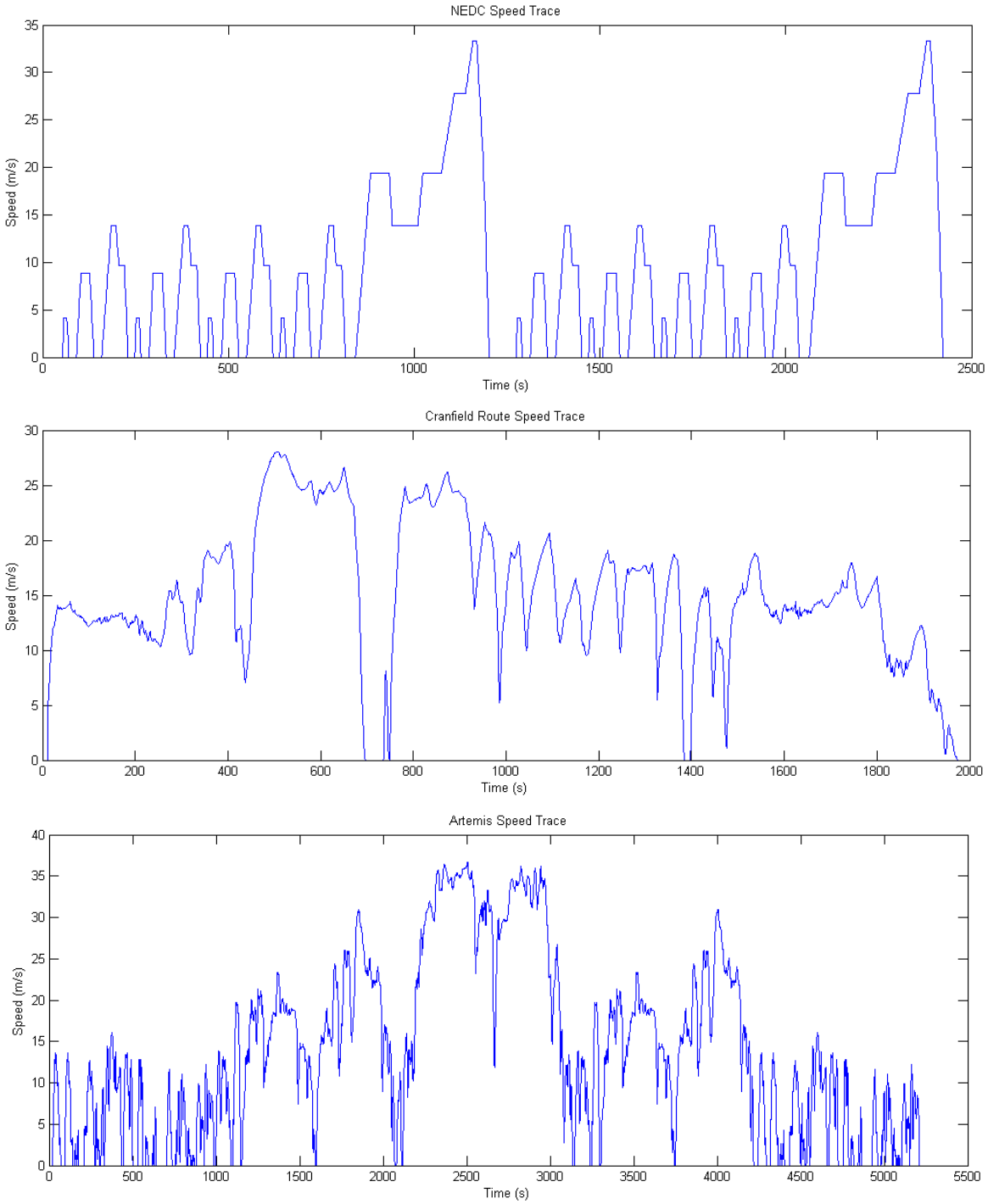

Appendix A3

Figure A2. Simulink model of the MPS.

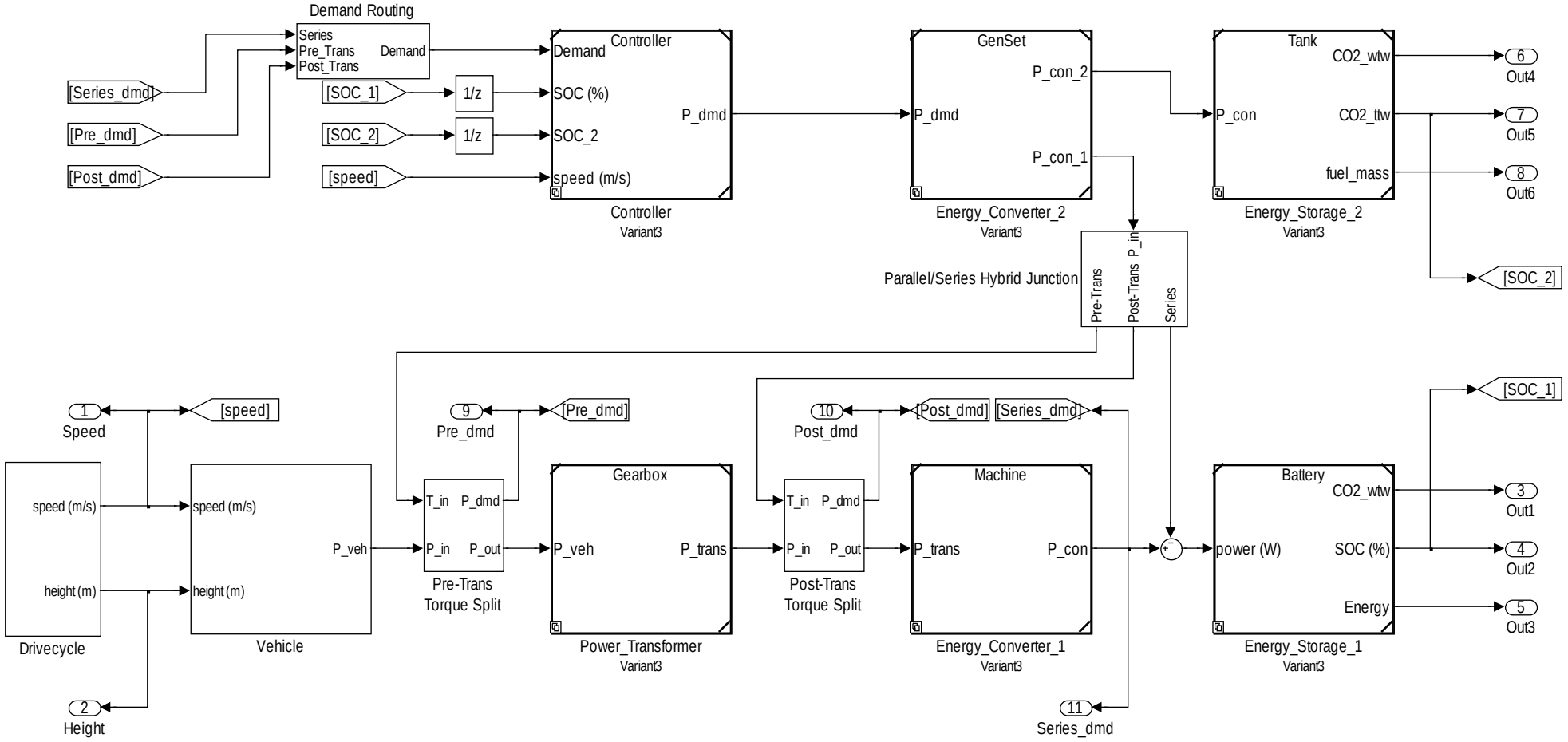

Appendix A4. Further discussion on behavior of normalized well-to-wheel CO_2 emission per kilometer

To aid this discussion, Figure A3a shows the well-to-wheel CO_2 emissions for the EV used in Case Study 1. The EV was optimized for lowest well-to-wheel CO_2 over an incremental travel range on the NEDC. Extended travel range was obtained by repeating the NEDC back-to-back. An example of this can be seen in Figure A3, where the NEDC was repeated twice. In Figure A3a, the blue line represents the normalized well-to-wheel CO_2 output in grams per kilometer, whereas the green line represents the accumulated (total) well-to-wheel CO_2 output in kilograms.

Figure A3. (**a**) Well-to-wheel CO_2; and (**b**) end-of-journey battery state of charge (SOC) as a function of travel range.

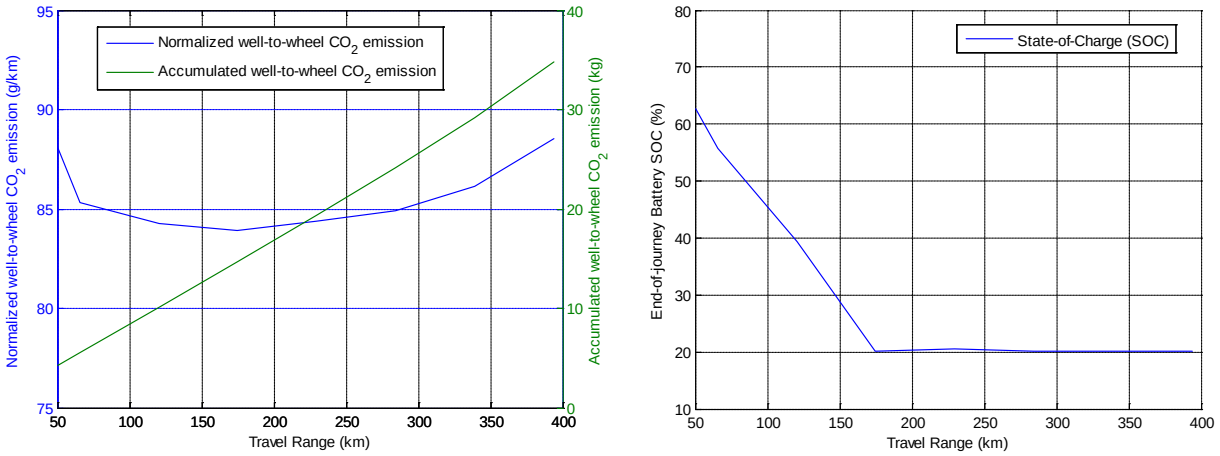

(**a**) (**b**)

Referring to Figure A3a, it is noteworthy that the lowest point for the normalized CO_2 output occurs when the EV is optimized for a travel range of 175 km. When the EV is optimized for a larger travel range (more than 175 km), the normalized CO_2 emission rises accordingly. This is caused by the increase in vehicle mass, which is mainly driven by the increase in battery size to satisfy the larger travel range. Consequently, as the vehicle mass increases, more energy is required to propel the EV over the drive cycle. Hence, the larger the travel range that the EV is optimized for, the greater the amount of CO_2 is emitted per kilometer.

However, it is also noticeable that the normalized CO_2 output rises again when the EV is optimized for travel ranges smaller than 175 km. In this scenario, the battery was identified to be "oversized" for travel ranges below 175 km. This is validated in Figure A3b, where it is observed that the battery does not discharge to the minimum limit of 20% SOC during such shorter travel ranges. If the battery were made smaller to maximize on its SOC range, its C-rate limit will be approached or exceeded, because the peak power demand from the drive cycle is almost constant, regardless of travel range. Therefore, although the accumulated well-to-wheel CO_2 emission is lower for shorter travel ranges, the normalized CO_2 emissions is inevitably higher because the battery is underutilized and its extra capacity is considered as "dead weight". A similar trend is also observed in Figure 19a. However, it ought to be mentioned that the characteristics shown in Figure A3 will vary depending on the battery C-rate

capability and vehicle glider mass, along with other assumptions made in this investigation such as the regenerative braking strategy.

Appendix A5.

Figure A4. Breakdown of vehicle mass for each powertrain architecture (correlates with Figure 20).

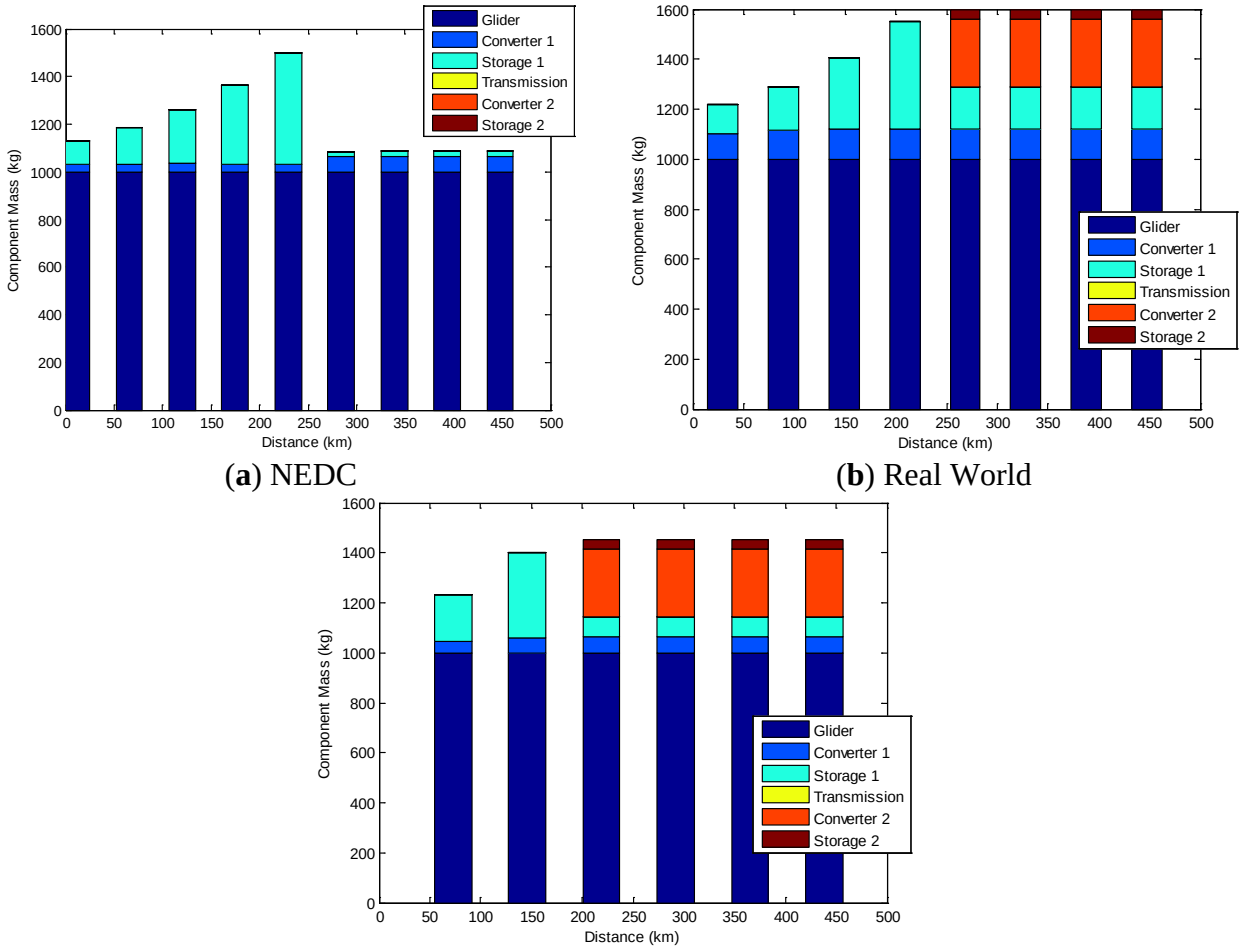

(**a**) NEDC (**b**) Real World

(**c**) Artemis

Acknowledgments

The powertrain components were parameterized based on data gathered from literature review and work carried out for the following consortiums:

- Smart Move 2 Electric Vehicle Trial conducted by Cenex;
- FUTURE Vehicle consortium (EPSRC grant number EP/I038586/1).

The authors wish to thanks these consortiums for their funding and continued support.

Conflicts of Interest

The authors declare no conflict of interest.

References

1. Li, X.; Williamson, S.S. Comparative Investigation of Series and Parallel Hybrid Electric Vehicle (HEV) Efficiencies Based on Comprehensive Parametric Analysis. In Proceedings of the IEEE Vehicle Power and Propulsion Conference (VPPC), Arlington, TX, USA, 9–12 September 2007; pp. 499–505.
2. Diamond, D. The impact of government incentives for hybrid-electric vehicles: Evidence from US states. *Energy Policy* **2009**, *37*, 972–983.
3. Fontaras, G.; Pistikopoulos, P.; Samaras, Z. Experimental evaluation of hybrid vehicle fuel economy and pollutant emissions over real-world simulation driving cycles. *Atmos. Environ.* **2008**, *42*, 4023–4035.
4. Shankar, R.; Marco, J.; Assadian, F. A Methodology to Determine Drivetrain Efficiency Based on External Environment. In Proceedings of the IEEE Electric Vehicle Conference (IEVC), Greenville, SC, USA, 4–8 March 2012; pp. 1–6.
5. Shankar, R.; Marco, J.; Assadian, F. The novel application of optimization and charge blended energy management control for component downsizing within a plug-in hybrid electric vehicle. *Energies* **2012**, *5*, 4892–4923.
6. Chan, C.C. The state of the art of electric, hybrid, and fuel cell vehicles. *IEEE Proc.* **2007**, *95*, 704–718.
7. Milliken, W.F.; Milliken, D.L.; Metz, L.D. *Race Car Vehicle Dynamics*; SAE International: Warrendale, PA, USA, 1995; Volume 146.
8. Walker, A.; McGordon, A.; Hannis, G.; Picarelli, A.; Breddy, J.; Carter, S.; Vinsome, A.; Jennings, P.; Dempsey, M.; Willows, M. A Novel Structure for Comprehensive HEV Powertrain Modelling. In Proceedings of the IEEE Vehicle Power and Propulsion Conference (VPPC), Windsor, UK, 6–8 September 2006; pp. 1–5.
9. Salisa, A.R.; Zhang, N.; Zhu, J.G. A comparative analysis of fuel economy and emissions between a conventional HEV and the UTS PHEV. *IEEE Trans. Veh. Technol.* **2011**, *60*, 44–54.
10. Nzisabira, J.; Louvigny, Y.; Duysinx, P. Comparison of Ultra Capacitors, Hydraulic Accumulators and Batteries Technologies to Optimize Hybrid Vehicle Ecoefficiency. In Proceedings of the International Conference on Power Engineering, Energy and Electrical Drives, Lisbon, Portugal, 18–20 March 2009; pp. 353–358.
11. Ribau, J.; Silva, C.; Brito, F.P.; Martins, J. Analysis of four-stroke, wankel, and microturbine based range extenders for electric vehicles. *Energy Convers. Manag.* **2012**, *58*, 120–133.
12. Mohan, G.; Assadian, F.; Marco, J. Influence of Cost Function on EV Powertrain Sizing. In Proceedings of the Powertrain Modelling and Control Conference, Bradford, UK, 4–6 September 2012.
13. Mason, B.A.; Ebrahimi, M.; Farid, M. Reconfigurable modelling for drivetrain real-time simulation. *Proc. Inst. Mech. Eng. Part K J. Multi-Body Dyn.* **2009**, *223*, 309–323.
14. Karnopp, D.C.; Margolis, D.L.; Rosenberg, R.C. *System Dynamics: Modeling, Simulation, and Control of Mechatronic Systems*; Wiley-Interscience: New York, NY, USA, 2012.
15. Bandivadekar, A. *On the Road in 2035: Reducing Transportation's Petroleum Consumption and GHG Emissions*; Massachusetts Institute of Technology: Cambridge, MA, USA, 2008.

16. Contestabile, M.; Offer, G.J.; Slade, R.; Jaeger, F.; Thoennes, M. Battery electric vehicles, hydrogen fuel cells and biofuels. Which will be the winner? *Energy Environ. Sci.* **2011**, *4*, 3754–3772.
17. Guzzella, L.; Sciarretta, A. *Vehicle Propulsion Systems: Introduction to Modeling and Optimization*; Springer: Berlin, Germany, 2005.
18. Rizzoni, G.; Guzzella, L.; Baumann, B.M. Unified modeling of hybrid electric vehicle drivetrains. *IEEE/ASME Trans. Mechatron.* **1999**, *4*, 246–257.
19. Zytek Automotive. Zytek IDT 120-55 Integrated 55 kW Electric Engine. Available online: http://www.zytekautomotive.co.uk/products/electric-engines/55kw (accessed on 23 February 2011).
20. Tremblay, O.; Dessaint, L.A.; Dekkiche, A.I. A Generic Battery Model for the Dynamic Simulation of Hybrid Electric Vehicles. In Proceedings of the IEEE Vehicle Power and Propulsion Conference (VPPC), Arlington, TX, USA, 9–12 September 2007; pp. 284–289.
21. He, H.; Xiong, R.; Fan, J. Evaluation of lithium-ion battery equivalent circuit models for state of charge estimation by an experimental approach. *Energies* **2011**, *4*, 582–598.
22. Plett, G.L. Extended Kalman filtering for battery management systems of LiPB-based HEV battery packs: Part 1. Background. *J. Power Sources* **2004**, *134*, 252–261.
23. Powell, B.K.; Pilutti, T.E. A Range Extender Hybrid Electric Vehicle Dynamic Model. In Proceedings of the 33rd IEEE Conference on Decision and Control, Lake Buena Vista, FL, USA, 14–16 December 1994; Volume 3, pp. 2736–2741.
24. Harrington, C.M. Vehicle Supervisory Control Task 6.1: Reusable Reference Architecture. In Proceedings of the Low Carbon Vehicle Technology Project (LCVTP) Workstream 6 Dissemination, Warwick Manufacturing Group (WMG), Warwickshire, UK, 21 January 2012.
25. *Government GHG Conversion Factors for Company Reporting*; Department for Environment, Food and Rural Affairs (DEFRA) and Department for Energy and Climate Change: London, UK, 2013.
26. Lucas, A.; Neto, R.C.; Silva, C.A. Energy supply infrastructure LCA model for electric and hydrogen transportation systems. *Energy* **2013**, *56*, 70–80.
27. Liberman, M.A. *Introduction to Physics and Chemistry of Combustion: Explosion, Flame, Detonation*; Springer: Berlin, Germany, 2008.
28. *Inventory of US Greenhouse Gas Emissions and Sinks: 1990–2009*; United States Environmental Protection Agency (EPA): Washington, DC, USA, 2011.
29. Moawad, A.; Singh, G.; Hagspiel, S.; Fellah, M.; Rousseau, A. Impact of Real World Drive Cycles on PHEV Fuel Efficiency and Cost for Different Powertrain and Battery Characteristics. In Proceedings of the International Battery, Hybrid, and Fuel Cell Electric Vehicle Symposium (EVS24), Stavanger, Norway, 13–16 May 2009.
30. Wirasingha, S.G.; Emadi, A. Classification and review of control strategies for plug-in hybrid electric vehicles. *IEEE Trans. Veh. Technol.* **2011**, *60*, 111–122.
31. Shankar, R.; Marco, J.; Assadian, F. Design of an Optimized Charge-Blended Energy Management Strategy for a Plugin Hybrid Vehicle. In Proceedings of the International Conference on Control UKACC, Cardiff, UK, 3–5 September 2012; pp. 619–624.
32. Pourabdollah, M.; Murgovski, N.; Grauers, A.; Egardt, B. Optimal sizing of a parallel PHEV powertrain. *IEEE Trans. Veh. Technol.* **2013**, *62*, 2469–2480.

33. Sundstrom, O.; Guzzella, L.; Soltic, P. Torque-assist hybrid electric powertrain sizing: From optimal control towards a sizing law. *IEEE Trans. Control Syst. Technol.* **2010**, *18*, 837–849.
34. Wipke, K.B.; Cuddy, M.R.; Burch, S.D. ADVISOR 2.1: A user-friendly advanced powertrain simulation using a combined backward/forward approach. *IEEE Trans. Veh. Technol.* **1999**, *48*, 1751–1761.
35. Barlow, T.J.; Latham, S.; McCrae, I.S.; Boulter, P.G. *A Reference Book of Driving Cycles for Use in the Measurement of Road Vehicle Emissions*; TRL Limited: Berkshire, UK, 2009; Volume 1.
36. Silva, C.; Ross, M.; Farias, T. Evaluation of energy consumption, emissions and cost of plug-in hybrid vehicles. *Energy Convers. Manag.* **2009**, *50*, 1635–1643.
37. Ribau, J.P.; Sousa, J.M.C.; Silva, C.M. Plug-in hybrid vehicle powertrain design optimization: Energy consumption and cost. *Lect. Notes Electr. Eng.* **2013**, *191*, 595–613.
38. Harrington, C.M.; Marco, J.; Vaughan, N.D. The design of a reference control architecture to support vehicle hybridisation. *Int. J. Veh. Des.* **2012**, *60*, 206–224.
39. Lampinen, J. Cam shape optimisation by genetic algorithm. *Comput.-Aided Des.* **2003**, *35*, 727–737.
40. Fang, L.; Qin, S.; Xu, G.; Li, T.; Zhu, K. Simultaneous optimization for hybrid electric vehicle parameters based on multi-objective genetic algorithms. *Energies* **2011**, *4*, 532–544.
41. Ribau, J.; Sousa, J.; Silva, C. Multi-Objective Optimization of Fuel Cell Hybrid Vehicle Powertrain Design—Cost and Energy. In Proceedings of the 11th International Conference on Engines & Vehicles, Capri, Italy, 11–15 September 2013.
42. Goldberg, D.E. *Genetic Algorithms in Search, Optimization and Machine Learning*; Addison-Wesley Longman Publishing Co.: Boston, MA, USA, 1989.
43. Ferreira Pinto, A.S.A. Evolution of Weight, Fuel Consumption and CO_2. Master's Thesis, Instituto Superior Tecnico, Lisbon, Portugal, 2009.
44. Fischer, M.; Werber, M.; Schwartz, P.V. Batteries: Higher energy density than gasoline? *Energy Policy* **2009**, *37*, 2639–2641.
45. Smart USA Smart Electric Drive. Available online: http://www.smartusa.com/models/electric-drive/overview.aspx (accessed on 23 February 2012).